Pressure-Induced Changes in Astrocyte GFAP, Actin and Nuclear Morphology in Mouse Optic Nerve

Yik Tung Tracy Ling[1], Mary E. Pease[2], Joan L. Jefferys[2], Elizabeth C. Kimball[2], Harry A. Quigley[2], and Thao D. Nguyen[1]

[1]*Department of Mechanical Engineering, The Johns Hopkins University, Baltimore, MD 21218, USA*
[2]*Wilmer Ophthalmological Institute, Johns Hopkins School of Medicine, Baltimore, MD 21287, USA*

Abstract

Purpose: To conduct quantitative analysis of astrocytic GFAP, actin and nuclei distribution in mouse optic nerve (ON) and investigate changes in the measured features after 3-day ocular hypertension (OHT).

Method: Serial cross-sections of 3-day OHT and control ONs were fluorescently labelled and imaged using confocal microscope. Eighteen structural features were measured from the acquired images, including GFAP coverage, actin area fraction, process thickness, and aspect ratio of cell nucleus. The measured features were analyzed for variations with axial locations along ON and radial zones transverse to ON, as well as for the correlations with degree of IOP change.

Results: The most significant changes in structural features after 3-day OHT occurred in the unmyelinated ON region (R1), and the changes were greater with greater IOP elevation. While GFAP, actin, axonal and ON areas all increased in 3-day OHT ONs in R1 ($P \leq 0.004$ for all), the area fraction of GFAP actually decreased ($P = 0.02$), the actin area fraction was stable and individual axon compartments were unchanged in size. Within R1, the number of nuclear clusters increased ($P < 0.001$), but the mean size of nuclear clusters was smaller ($P = 0.02$) and the clusters became rounder ($P < 0.001$). In all cross sections of control ONs, astrocytic processes were thickest in the rim zone compare to the central and peripheral zones ($P < 0.001$ for both); while the overall process width in R1 decreased after 3-day OHT ($P < 0.001$).

Conclusion: The changes in structure elucidate IOP-generated alterations that underlie astrocyte mechanotranslational responses relevant to glaucoma.

Pages: 30 , *Word Count: 5937*,
Keywords: optic nerve head, GFAP, actin, IOP elevation, nucleus, astrocytes *Supported by:* NIH EY

02120 (Dr. Quigley); EY 01765 (Core facility grant, Wilmer Institute); NSF Award 1727104; Brightfocus Foundation G2015132; and the Croucher Foundation (YTTL).

1 Introduction

Glaucoma is an ocular disease characterized by regional visual loss due to gradual degeneration of retinal ganglion cell (RGC) axons at the optic nerve head (ONH)[1]. In human and large mammalian eyes, the ONH contains supportive connective tissue beams covered by astrocytes, referred to as the lamina cribrosa (LC). RGC axon bundles pass through openings between the beams and fine astrocyte processes encircle axons in LC openings. The external ONH border is delimited at the exit from the retina by Bruch's membrane opening (BMO). The LC in rodents, smaller by an order of magnitude in diameter than the human, is spanned by astrocytes with minimal connective tissue, but with a comparable 3-dimensional network structure similar to the human. The mouse astrocytic lamina extends from the BMO to $\sim 240\ \mu m$ posteriorly, in an unmyelinated section of the optic nerve (ON). Further cephalad, the mouse ON axons acquire myelin. In large mammals, by contrast, myelination begins at the posterior border of the LC.

The level of intraocular pressure (IOP) is a key risk factor for glaucoma, the higher the IOP, the more likely and the more severely progressive is the damage[2]. Higher IOP is accompanied by axonal degeneration, which is preceded by blockage of axonal transport in both human eyes[3] and in animal models[4–8]. The exact mechanisms linking IOP to axonal damage have not been fully delineated, but the translation of IOP into mechanical stress at the ONH has been extensively studied and modeled[9–11]. Increase in IOP is postulated to produce trans-LC axial stress and circumferential hoop stress on the LC. Astrocytes bridge the mouse ONH and are anchored by peripheral processes to the peripapillary sclera. The structure suggests that astrocytes are important for sensing and translating mechanical stress into beneficial and pathological events for the enclosed axons. The astrocytic network also serves to modulate ionic balance, store neuroactive substances, optimize neuronal signaling, regulate blood flow and provide hexose nutrition to axons[12–14]. The cytoskeleton of astrocytes consists of co-existing filaments of actin and intermediate filaments.

Changes in astrocyte morphology in glaucoma models have been reported, primarily through immunolabeling of glial fibrillary acidic protein (GFAP), an intermediate filament component in astrocytes. Thickening

and thinning of processes[15,16], development of new processes along the ON axis[17] and reorganization of filaments[18] have been shown after different time points of axonal insult. Tehrani et al showed reorientation of actin-labelled astrocyte processes from a direction transverse to the ON axis to that along the ON axis[19]. Both GFAP and actin contribute significantly to astrocyte stiffness and morphology, while actin is also involved with force production, and vesicle mobility[20–22]. Studying GFAP, actin and nuclei of ONH astrocytes will likely improve knowledge of mechanisms leading to axonal degeneration.

This study provides detailed and quantitative measurement of the cytoskeletal network by analyzing fluorescently labelled mouse ON sections after 3-day ocular hypertension (OHT), and outlining the axial and radial differences in the ON. Previous morphological studies of astrocytes in glaucoma research have often used cultured cells or tissue sections of the ON, from which conclusions about the overall astrocytic network in the intact tissue are difficult to discern. Aligning observations relative to an anatomical reference and providing indicators for morphological variations may aid future comparisons across studies. Serial ON sections were imaged after immunolabeling or staining for GFAP, actin and DAPI. A custom morphological algorithm[23] was adapted to quantify structural features, including area coverage, process thickness and aspect ratio of nuclei. The outcomes were used to examine differences after 3-day OHT nerves and to assess the effect of IOP level. Our purpose was to develop methods that will reveal alterations in mechanobiological support to axons and to advance understanding of IOP-induced mechanical changes that contribute to axonal insults.

2 Methods

The following section summarizes in detail the methods in specimen preparation, image processing and network analysis used to identify and quantify the features of the ON network structure, as well as the statistical methods for analysis of regional variations, and correlations between measured changes and degree of IOP elevation. Experimental protocols were approved by the Animal Care and Use Review Board of Johns Hopkins University School of Medicine. Mice were handled in a manner consistent with the ARVO Statement for the Use of Animals in Ophthalmic and Vision Research, and the Guide for the Care and Use of Laboratory Animals (Institute of Laboratory Animal Resources, the Public Health Services Policy on

Humane Care and Use of Laboratory Animals).

2.1 Specimen Preparation

Six 6-month old genetically modified mice expressing green fluorescent protein (GFP) driven by the glutamate transporter protein 1 (GLT1) promoter[24] (acquired from Jeffrey Rothstein, Johns Hopkins School of Medicine[25]) were used for this study. IOP elevation was induced unilaterally by injecting microspheres consisting of 2 μL of 6μm diameter beads, 2 μL of 1μm diameter beads and 1 μL of viscoelastic compound (10 mg/mL sodium hyaluronate, Healon; Advanced Medical Optics, Inc.)[26]. The fellow eyes served as contralateral controls. All mice were anesthetized with 75 mg/kg of ketamine, 10 mg/kg xylazine and 2 mg/kg acepromazine after 3 days of IOP elevation. The IOP was measured with a TonoLab tonometer (TioLat Inc) before bead injection and before sacrificing (Table 1). The difference in IOP between the 3-day treated and control eyes of each mouse was recorded as the IOP difference (ΔIOP). In previous large scale experiments, we found that the IOP one day after bead injection is often substantially higher than that at 3 days, and more than 95% of bead-injected eyes achieve elevated IOP. For this experiment, we avoided the potential effect of closely repeated anesthesia by not measuring IOP 1-day after bead injection.

For sacrifice, mice were exsanguinated under general anesthesia as above, then perfused with 4% paraformaldehyde in Sorenson's phosphate buffer before enucleation. The globes were immersed in the same fixative for an hour and were transferred into 0.1M PO4 buffer, where the extraocular tissues were removed. An ON segment 1mm in length was separated from the posterior eye wall using a sharp razor blade and embedded in a mixture of 20% sucrose-buffer and OCT using a modified protocol from Barthel and Raymond[27]. The cryo-embedded segment was further sectioned into 8 or 10 μm slices starting from the posterior part of the ON using Cryostat CM3050S (Leica Biosystems) at -25 ^{o}C. ON sections were collected onto glass microscope slides. Sections that were folded or torn during cryosectioning were excluded from analysis.

2.2 Immunolabeling and staining

For immunolabeling, ON sections were first immersed in 2% normal goat serum and 0.1% Triton X-100 in PBS solution to improve specificity and penetration of antibody. For GFAP labeling, sections were incubated

Table 1: Mouse optic nerves used for labeling of GFAP, actin and nuclei

Mouse ID	Gender	Eye	Initial IOP (mmHg)	Final IOP (mmHg)	Difference in Final IOP (ΔIOP, mmHg)
1	Male	Left	9	23	9
		Right	11	14	
2	Male	Left	7	22	7
		Right	10	15	
3	Male	Left	7	19	8
		Right	8	11	
4	Male	Left	8	16	8
		Right	14	8	
5	Female	Left	13	13	-1
		Right	14	14	
6	Female	Left	17	19	4
		Right	14	15	

with primary rabbit anti-GFAP antibody (1:1000, Abcam AB7260) overnight at 4^oC in a humid chamber in the dark followed by secondary Alexa Fluor 488 goat anti-rabbit antibody (1:500, Invitrogen A11008) for 1 hour at room temperature. ONH sections were also incubated with Alexa Fluor 568 phalloidin (1:60, Invitrogen A1280) for 20 mins to reveal actin filaments and DAPI (1:1000, Roche 10-236-276-001) for 1 hour for staining nuclei. All sections were mounted with Dako mounting media and covered with glass cover slips for imaging.

2.3 Image Acquisition

Confocal fluorescent images were obtained with a Zeiss LSM 710 confocal microscope using a Plan-Apochromat 40x oil-immersion objective. Three channels of images at excitation wavelength of 458 nm for GFAP, 561 nm for actin, and 405 nm for nuclei (Figure 1) were captured for each ONH section. The z-position (depth within a section) was selected close to the surface, where signals from all three channels are visible. Each channel consisted of 3 by 3 tiled images that were stitched with a 12% overlap. The resulting images with a resolution 0.1038 μm/pixel were exported as TIFF files for structural characterization. During acquisition, the section immediately posterior to the level of retinal photoreceptor nuclei was marked as the position of BMO. Quantitative image processing was conducted on all images posterior to the BMO, which comprised

ON lengths ranging from 640 μm to 960 μm.

2.4 Image Processing

Images were pre-processed with a 3 x 3 median filter to reduce noise and with contrast-limited adaptive histogram equalization (CLAHE)[28] to enhance contrast of acquired signals (Figure 1). All three channels were individually binarized using the Otsu thresholding method[29], such that the actin, GFAP and nuclear fluorescent regions were represented as 1, while the background pixels were labelled as 0. An ON boundary was automatically detected from the binarized GFAP image by filling in spaces bounded by GFAP signals, and tracing the outermost boundary of the filled region. An average of 8 sections across each ON had overestimated auto-traced boundaries due to inclusion of connecting peripapillary sclera and thus were manually corrected. The ON boundary coordinates were used to extract the area of interest in actin and nuclei channels as well. A series of morphological smoothing was performed to remove local artifacts due to binarization, adapted from a previously reported method[23,30]. These included using 'bwmorph' with the options of 'clean', 'majority', 'bridge' to remove pixel-level noise. Morphologic opening (Matlab function 'imopen') was also applied with disk element sizes of 3 and diamond element size of 4 in the GFAP and nuclei channels, respectively, to separate regions that were partly connected. The resulting binarized images were used to measure the structural parameters in each cross-section. For verification of the binarization method, one local region of size 20 x 20 μm on the section 160 - 170 μm away from BMO of all ONs was selected for manual segmentation of the DAPI signals. Similarly, a local region of size 5 x 5 μm was manually traced on the GFAP and actin images as well. The manual segmentations were compared to that from the image processing algorithm by calculating the percentage differences in the resulting area fractions. The calculation of area fraction is described in detail in the Structural Measurements section.

2.5 Structural Measurements

A total of 18 structural features were measured using a custom code in Matlab R2019a (MathWorks, Inc., Natick, MA): 6 each from GFAP and nuclei channels, 3 from the actin channel, and additional 3 from the negative space of actin and nuclei images, which represented the axonal space. The measured features were defined as follows:

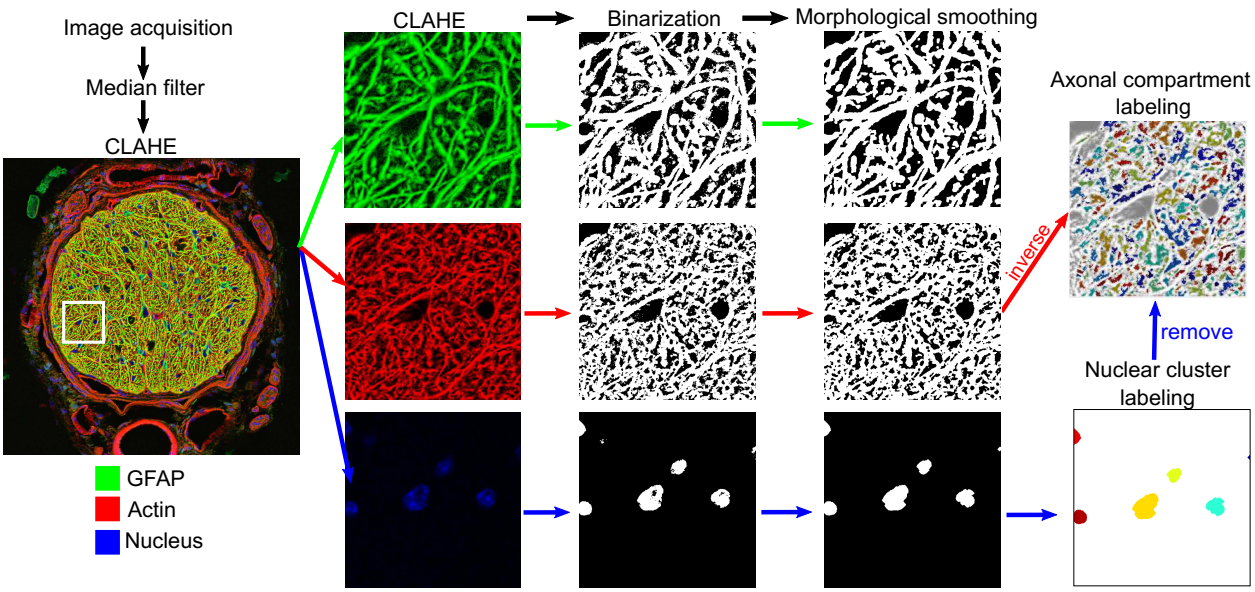

Figure 1: A series of image processing steps were applied to the fluorescent images to measure the features of the optic nerve. The fluorescent image was post-processed using a median filter and CLAHE and the results are shown in a $42\mu m \times 42\mu m$ area for GFAP, actin and nuclear channel. Each channel was then binarized using the Otsu thresholding method[29] and morphologically smoothed. The final binarized image of GFAP channel was used for structural measurements while that of actin and nucleus channel were further inverted to locate the axonal space. Each disconnected axonal space was randomly labelled as a separate axonal compartment and each isolated nuclear area was randomly labelled as a separate nuclear cluster for visualization.

- *ON area*: The total area within the detected ON boundary; the boundaries were highlighted in red lines in (Figure 3d).

- *ON aspect ratio*: The aspect ratio was determined by fitting an ellipse to the ON boundary and calculating the ratio of the major to minor axes.

- *GFAP, actin and nuclei area*: The total number of pixels labelled as foreground in each channel within ON boundary.

- *GFAP, actin and nuclei area fraction*: Area fractions were recorded as the GFAP, actin and nuclei area over the ON area.

- *GFAP process width*: Each binarized GFAP image was skeletonized using the Matlab function 'bwmorph' with options 'thin' and 'inf'. Skeletonization represents the middle line of each process with line width of 1 pixel. Process width at each skeleton pixel was measured as two times the shortest distance from the skeleton pixel to the boundary of the foreground. Average process width was calculated over all skeleton pixels in the area of interest. The average beam width was calculated both within ON and in each radial regions, as described in the section 2.6.

- *GFAP and actin process anisotropy*: A histogram of process orientations was first obtained by applying 2D discrete Fourier transform to the input image and then averaging the intensities of each pixel in a line segment that corresponded to the respective orientation[31]. A circular average of process orientation was then calculated using the Matlab circular statistics toolbox developed by Berens et al.[32]. The anisotropy of the processes was defined by fitting the semicircular von Mises probability density function to the histogram of orientation angles centered about the circular average orientation. The resulting dispersion parameter, which signifies the degree of alignment along the average orientation, was defined as the anisotropy[23]. A network with processes aligned in parallel with each other would yield an infinite dispersion value, while a dispersion value of 0 would indicate that the processes are not selectively aligned along any one direction.

- *Number of nuclear clusters* The number of separated regions in the DAPI labelled channel was recorded as the number of nuclear clusters per section (Figure 1).

- *Nuclear cluster density* The number of nuclear clusters per mm^2 was calculated to account of change in ON area (Figure 1).
- *Aspect ratio of nuclear clusters*: The ratio of major to minor axes of each nuclear cluster.
- *Axonal area*: The total area within the ON that was not labelled as actin or nuclei represented the axonal area.
- *Number of axonal compartments*: Number of disconnected regions in axonal area (Figure 1).
- *Mean area of axonal compartments*: The mean number of pixels in each axonal compartment.

2.6 Regional division

The optic nerves were divided lengthwise into 3 regions beginning at BMO. The first segment was the unmyelinated region (R1), defined by the distance 0-240 μm from the BMO. The second was the myelin transition region (R2), defined from 240-480 μm from the BMO and the third was the myelin region defined as >480 μm from the BMO (Figure 3a). These distances were based on the positions of these anatomical regions in images of both control and treated mouse ON[33]. Within each cross section, the ON was further divided into 3 radial zones: central, peripheral, and rim zones (Figure 2a). The zones were defined by first locating the center of mass of the ON (Matlab function 'regionprops' with options 'Centroid'), and then separating the ON by distances that were equal to 50% and 90% of the length from the center to the ON outer boundary.

2.7 Statistical analysis

The structural parameters (Table 2) measured from each ON section were averaged every 40 μm interval from BMO up to 640μm distally, amounting to 6 intervals each in R1 and R2, and 4 intervals in R3. A total of 9 intervals (4.7% of all intervals) had artifact that precluded analysis of the GFAP signals. Four of these intervals had corresponding actin and DAPI signals that were similarly affected and were excluded from further analysis. To eliminate the inter-mouse variations in control measurements, the ratio of 3d OHT over control eyes was calculated for each outcome in each interval to represent the fold change after

treatment. A ratio of 1 indicated that the outcome was the same between treated and control nerves and a ratio above 1 indicated an increase in the outcome in 3-day OHT eyes. The interval ratios were used to compare differences in structural outcomes after 3-day IOP elevation. In addition, we assessed the effect of the estimated IOP difference on the ratio in region R1. Both analyses used general linear models, which took into consideration the possible correlations among repeat ratios in multiple intervals for a single ON. The repeat measurements were assumed to have an autoregressive correlation structure, e.g. the closer two intervals are in distance from the retina, the higher the correlation. Note that since the GFAP and actin network were mostly isotropic, with the anisotropic dispersion values close to 0, leading to ratio values that were much greater than 1.47 fold, the median of all anisotropy ratio values. Therefore, anisotropy ratios that were above 4 fold were removed as outliers (9 intervals from GFAP and 10 intervals from actin), whilst the new median ratio value of 1.35 fold remained at a similar level.

For comparison of GFAP process width among central, peripheral and rim zones, all estimates and $P-$values were obtained from mixed linear models to account for the clustering of areas within each ON for a control eye as well as correlations among intervals. Again, intervals were assumed to have an autoregressive correlation structure. Bonferroni adjustment was implemented for $P-$values from multiple pairwise comparisons. All aforementioned analyses were performed using SAS 9.2 (SAS Institute, Cary, NC). In addition, to compare the difference in magnitude of ON, actin, GFAP, axonal and nuclear areas (Figure 5a), one-way analysis of variance (ANOVA) in Matlab by using function 'annova1' followed by 'multcompare' was used for the multiple comparison test.

3 Results

3.1 Measured features in control eyes

Across all sections of control ONs, the average ON area in control eyes was $0.051\pm0.008\ mm^2$, while the GFAP and actin areas covered 58.5% and 68.4% of the ON area (Figure 5c). The average number of nuclear clusters within the ON was 123 ± 28 per section, covering 6.8% of the ON area. The axonal compartments occupied 22.0% of the ON area (Figure 1f). The average astrocyte process width measured from the GFAP channel was $1.59 \pm 0.10\ \mu m$. Overall, astrocyte actin coverage in ON sections was greatest, followed by

GFAP, axonal area and nuclear area (Figure 5a).

In control nerves, the ON, GFAP and actin areas were lowest at the BMO. All three areas increased dramatically through R1, peaked in R2, and decreased slightly in R3 (Figure 3a-b & 4a). The GFAP area fraction in control nerves was greatest at BMO and declined through the length of ON (Figure 3c). The actin area fraction increased steadily though R1 and remained at similar level in R2 and R3 (Figure 4b). The actin channel showed more distinct and elongated bundles in R1, while the actin staining in R2 and R3 had less distinct bundles (Figure 4d-f & Supplement Figure S1). The total number of nuclear clusters increased from BMO through the myelinated region (Figure 4c & Supplement Figure S2), and the number of axonal compartments increased steadily in R1 and R2, but became stable in R3.

The average GFAP process width in the central zone of all control ONs was 9.2% thinner than in the rim zone, and in the peripheral zone processes were 8.6% thinner than in the rim zone ($P < 0.001$ for both comparisons, Figure 2a & c). The GFAP area fraction in the central zone (54.7%) was also lower than in the peripheral (59.3%) and the rim zone (68.6%, $P < 0.001$ for both comparisons, Figure 2b).

All cross-sectional structural outcomes were averaged every 40 μm intervals and separated into axial regions of R1, R2 or R3 (Table 2 and supplemental section Table S1 & S2) for comparison after 3-day OHT in the following section.

3.2 Change in parameters after 3-day OHT treatment

Across all measured features, the ratios between 3-day OHT and control nerves were similar between R2 and R3, while changes in R1 were most significant (Table 3), including increases in OHT ON area, actin area and axonal area and a decrease in GFAP area fraction. The increase in number of nuclear clusters and decrease in aspect ratio of the clusters were also larger in R1 than R2 ($P \leq 0.02$ for both). Thus, we will present in detail only further results in R1 after 3-day OHT treatment (Table 2).

The estimated mean areas of ON, GFAP and actin were 1.16, 1.12, and 1.15 times larger, respectively, for the 3-day OHT group than controls ($P < 0.01$, Figure 5). In addition, the axonal area and nuclear area were 1.13 ($P < 0.001$) and 1.27 times larger ($P = 0.02$) (Table 2). Since the increase in GFAP area was proportionately less than that of the ON area, there was a 5.3% decrease in GFAP area fraction ($P = 0.02$). The actin and nuclear area fractions remained unchanged. The GFAP process width decreased from 1.65

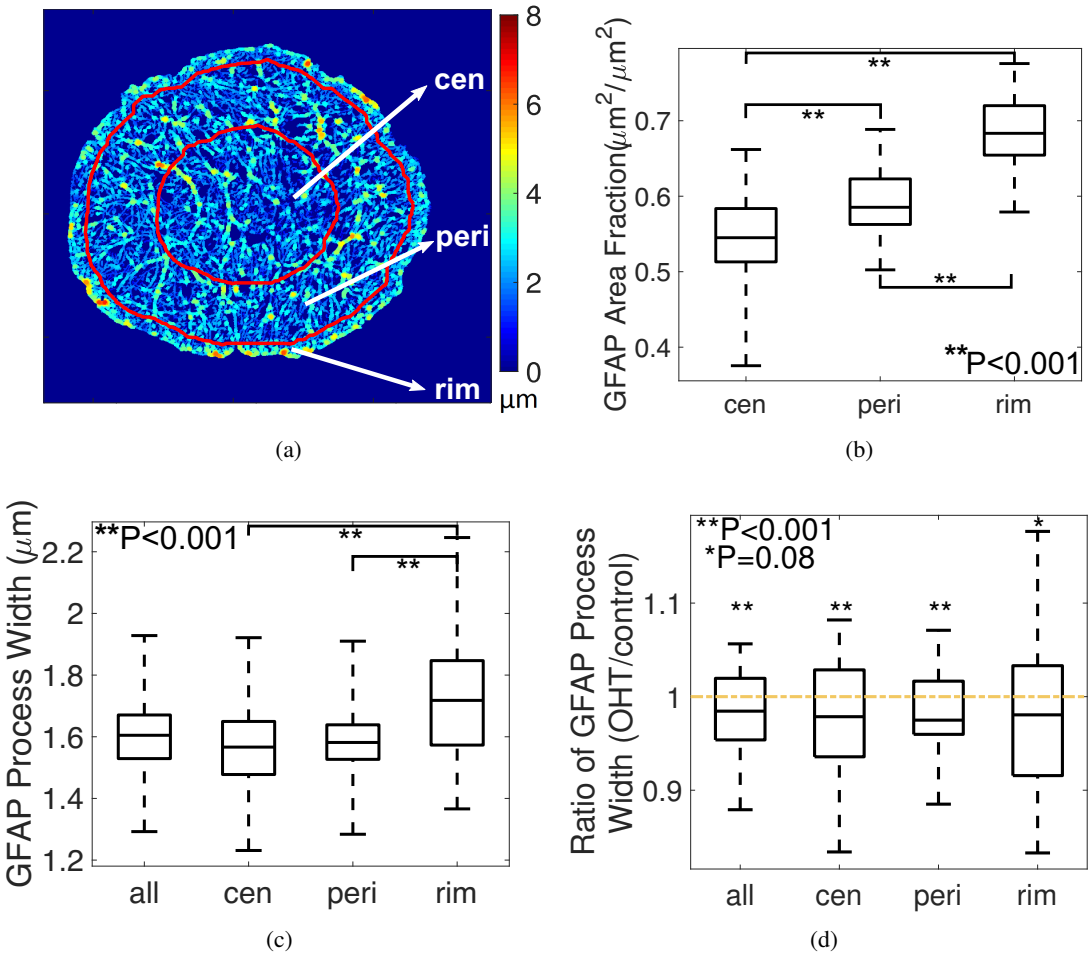

Figure 2: Radial variations in GFAP process width, showing (a) a color map of measured process width and regional divisions. Central zone (cen), peripheral (peri) and rim zone were divided as zones within 0-50%, 50-90% and 90-100% of radii from fitted center of the ON to the ON boundary. (b) Processes were thicker in the rim zone compare to central and peripheral zones ($P < 0.001$ for both pairwise comparisons from linear mixed model and after Bonferroni adjustment). (c) In R1, processes in all 3 zones became thinner after 3-day OHT than controls ($P = 0.08$ for the rim region and $^{**}P < 0.001$ for others).

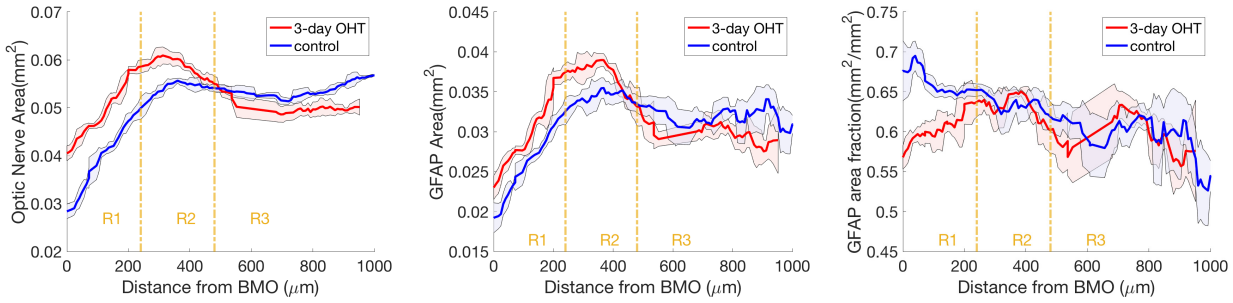

(a)

(b)

(c)

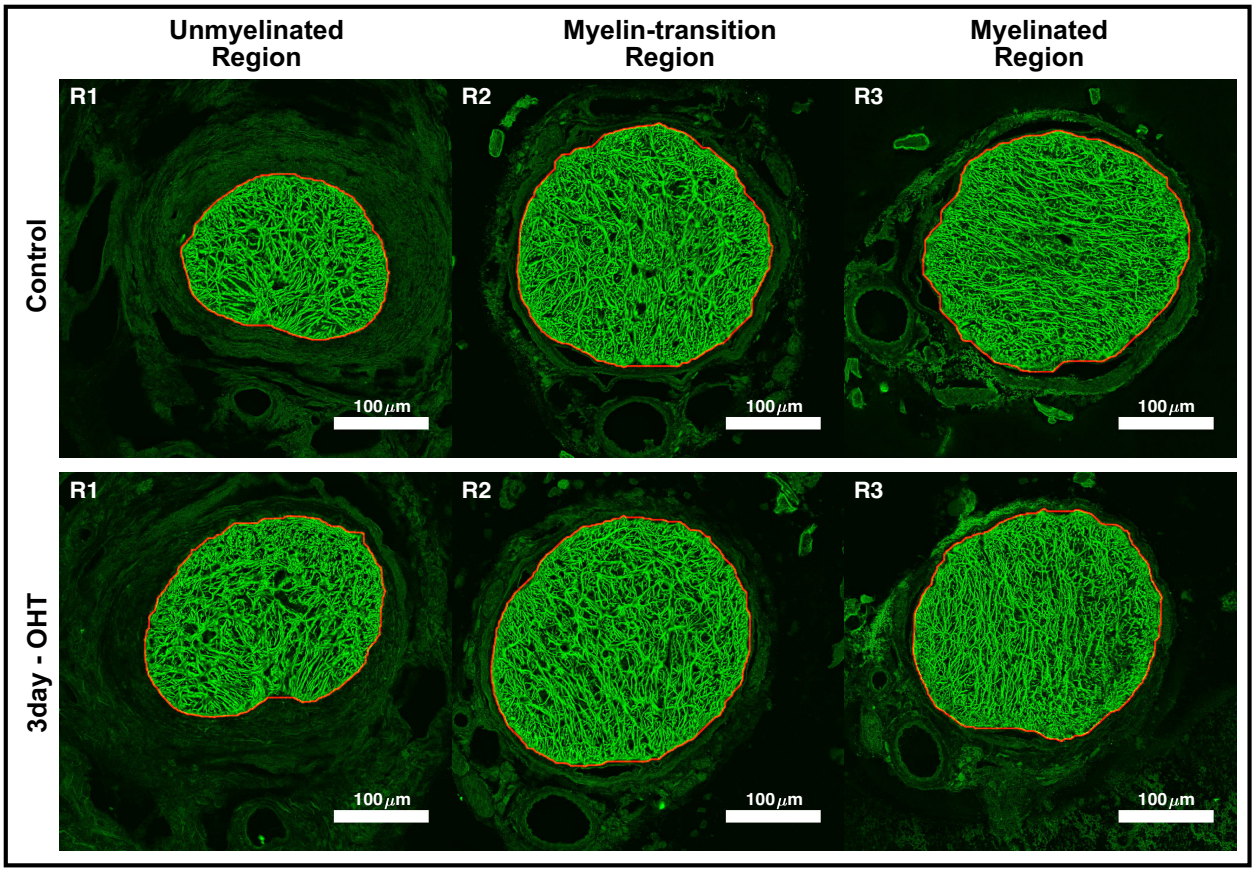

(d)

Figure 3: The axial variations of outcomes measured from the GFAP channel, showing the (a) ON area, (b) GFAP area and (c) GFAP area fraction of both control and 3-day ocular hypertension measurement from representative mouse 1. The colored lines represent the moving mean of 5 successive sections along the ON and the shaded areas represent the respective moving standard deviations. Separation of R1, R2 and R3 corresponds to the unmyelinated, myelin-transition and myelinated region of the ON. (d) Representative distance-matched pairs of GFAP-labelled control and OHT ONs after median filter and CLAHE were taken from each axial region of mouse 1. The mouse ON typically transitions from a kidney bean shape in R1 into an oval shape in R2 and R3.

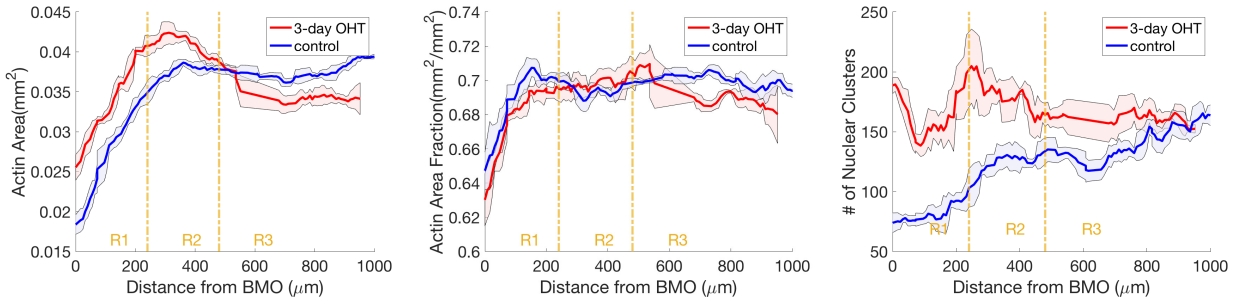

(a) (b) (c)

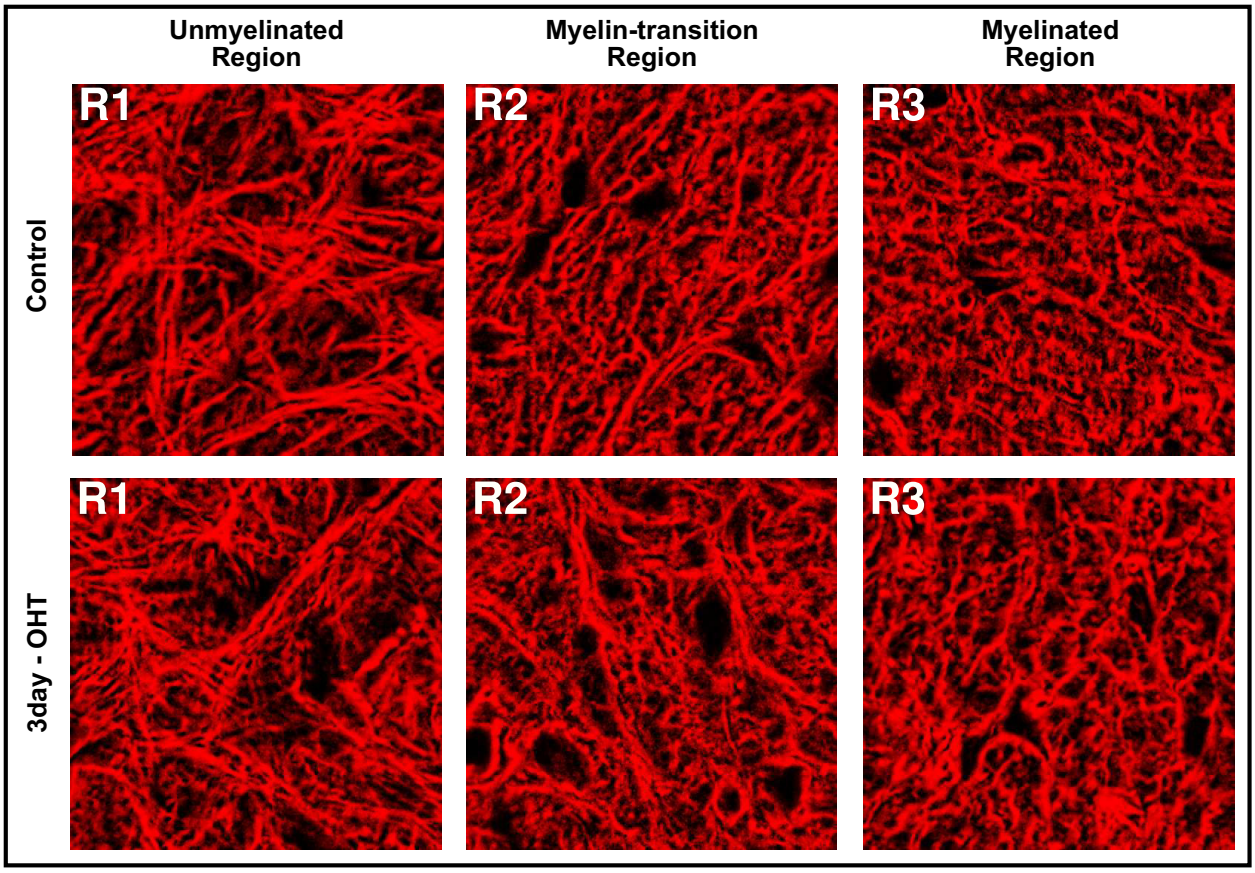

(d)

Figure 4: The axial variations of outcomes measured from the actin and nucleus channels, showing the (a) actin area, (b) actin area fraction and (c) number of nuclear clusters of both control and 3-day OHT measurement from representative mouse 1. The colored lines represent the moving mean of 5 successive sections along the ON and the shaded areas represent the respective moving standard deviations. Region R1, R2 and R3 correspond to the unmyelinated, myelin-transition and myelinated region of the ON. (d) A $42\mu m \times 42\mu m$ area of distance-matched pairs of control and 3-day OHT actin networks after median filter and CLAHE were taken from each region of the mouse 1. The actin fiber bundles were straighter and more distinct in R1 than in R2 and R3, where they take on a wavier appearance.

Table 2: Comparison of 3-day OHT and control ON parameters in R1.
Results of the general linear models for mean, standard deviation (std) and $P-$values for ratio of 3-day OHT over control different from 1, estimated ratios are listed in column 3 of Table 3. All measured areas were higher in 3-day OHT nerves. $P-$value ≤ 0.01 were highlighted as *, and those≤ 0.05 were marked with**.

	Measured Features	**Control $\pm$ std**	**3-day OHT $\pm$ std**	$P-$**value**
GFAP	Aspect Ratio of ON (mm/mm)	1.21 ± 0.08	1.26 ± 0.09	0.22
	ON Area (mm^2)	0.042 ± 0.008	0.049 ± 0.007	<0.001 **
	GFAP Area (mm^2)	0.026 ± 0.005	0.029 ± 0.005	0.004 **
	GFAP Area Fraction (mm^2/mm^2)	0.62 ± 0.02	0.60 ± 0.02	0.02 **
	GFAP Beam Anisotropy	0.11 ± 0.08	0.13 ± 0.07	< 0.001 **
	Process Width (μm)	1.65 ± 0.09	1.62 ± 0.06	<0.001 **
	Process Width - central (μm)	1.64 ± 0.11	1.60 ± 0.10	<0.001 **
	Process Width - peripheral (μm)	1.61 ± 0.10	1.58 ± 0.06	<0.001 **
	Process Width - rim (μm)	1.77 ± 0.09	1.72 ± 0.10	0.08 *
Actin	Actin Area (mm^2)	0.028 ± 0.006	0.033 ± 0.005	<0.001 **
	Actin Area Fraction (mm^2/mm^2)	0.68 ± 0.02	0.67 ± 0.02	0.11
	Actin Process Anisotropy	0.081 ± 0.059	0.082 ± 0.046	0.38
Axon	Axonal Area (mm^2)	0.009 ± 0.002	0.011 ± 0.002	<0.001 **
	# of Axonal Compartments (#/cross section)	6324 ± 2009	6996 ± 1949	0.001 **
	Mean Area of Axonal Compartments (μm^2)	1.56 ± 0.25	1.56 ± 0.16	1
Nuclei	Nuclear Area (mm^2)	0.003 ± 0.001	0.004 ± 0.001	0.02 **
	Nuclear Area Fraction (mm^2/mm^2)	0.071 ± 0.026	0.081 ± 0.024	0.12
	# of Nuclear Clusters (#/cross section)	86.66 ± 8.49	127.17 ± 14.05	<0.001 **
	Nuclear Cluster Density (#/mm^2)	2134.81 ± 394.19	2665.64 ± 516.92	0.005 **
	Mean Area of Nuclear Clusters (mm^2)	32.25 ± 5.43	30.05 ± 3.25	0.02 **
	Mean Aspect Ratio of Nuclear Clusters ($\mu m/\mu m$)	2.18 ± 0.15	2.03 ± 0.08	<0.001 **

μm to 1.62 μm ($P < 0.001$), and the percentage decrease in central zone (3.7%, $P < 0.001$) was larger than that in the peripheral zone (2.5%, $P < 0.001$, Figure 2c). Processes in the rim region were 2.1% thinner, but the observation was marginally significant ($P = 0.08$). The number of individual axonal compartments was 1.13 times larger ($P = 0.001$), but the average area of each compartment remained the same at 1.56 μm^2. The number of nuclear clusters increased from 87 to 127 per cross section ($P < 0.001$), while the mean cluster area decreased by 6.8% ($P = 0.02$). On average, nuclear clusters were less elongated, as their aspect ratio decreased from 2.18 to 2.03 $\mu m/\mu m$ ($P < 0.001$, (Figure 6). The GFAP processes were aligned more in parallel with each other after 3-day OHT, with an average dispersion of 0.11 in controls compare to 0.13 in OHT nerves (0 = completely isotropic, $P < 0.001$). The actin labelled processes alignment and ON aspect ratio were not significantly different after 3-day OHT treatment.

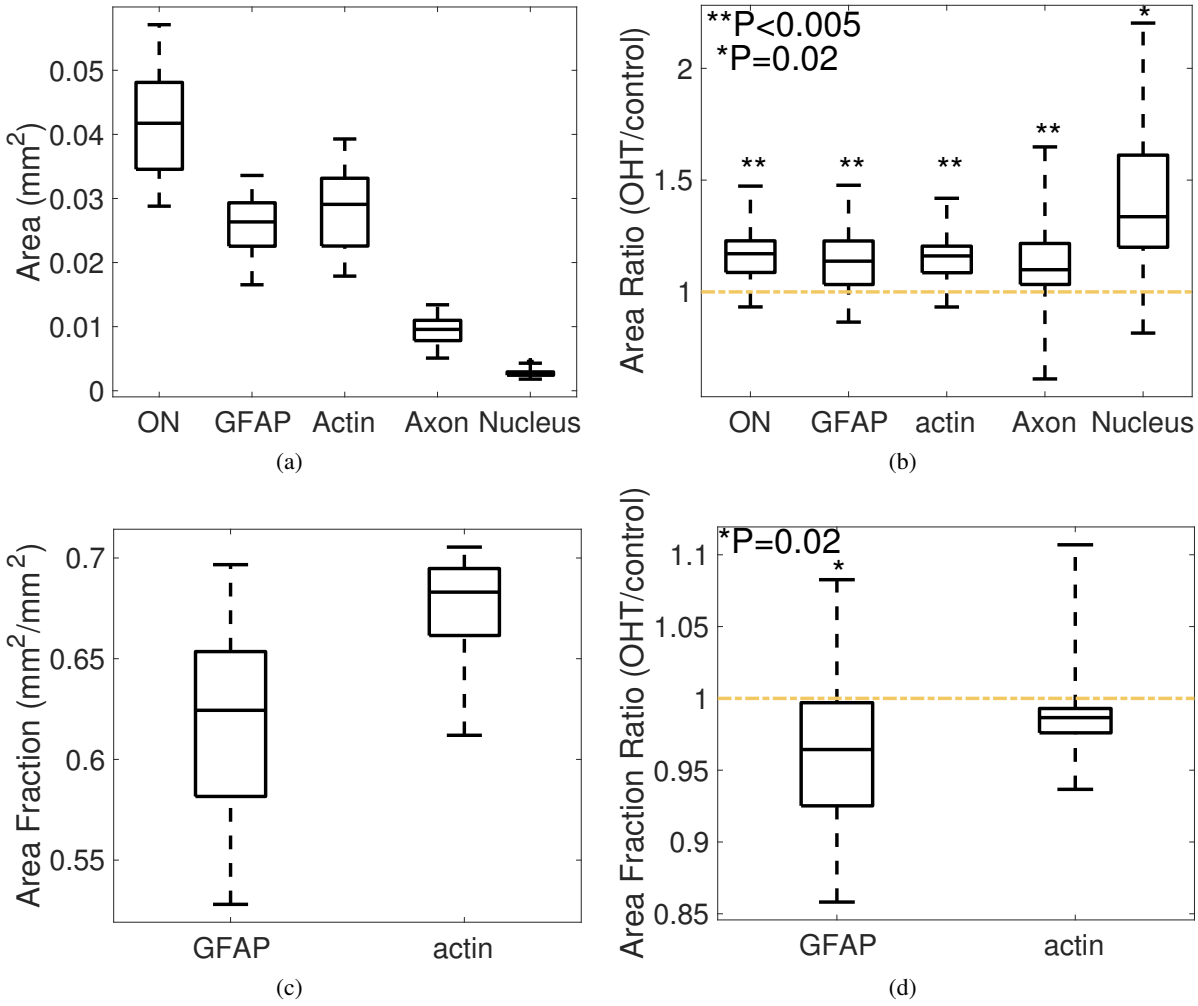

Figure 5: Comparison of parameter areas and area fractions (region R1) in control (left graphs) and change as a ratio between 3-day OHT and control ONs (right graphs). (a) Nuclear area is lowest compared to actin, GFAP and axonal areas. (b) All areas in R1 were greater in 3-day OHT ONs than in controls (ratio > 1). Nuclear area had the largest percentage increase (37%) after 3 days. (c) Control GFAP is somewhat lower than actin area fraction. (d) There is a significantly greater percentage decrease in GFAP area fraction over the change in actin area fraction after 3-day OHT treatment. $P-$values for (b) and (d) recorded from general mixed models.

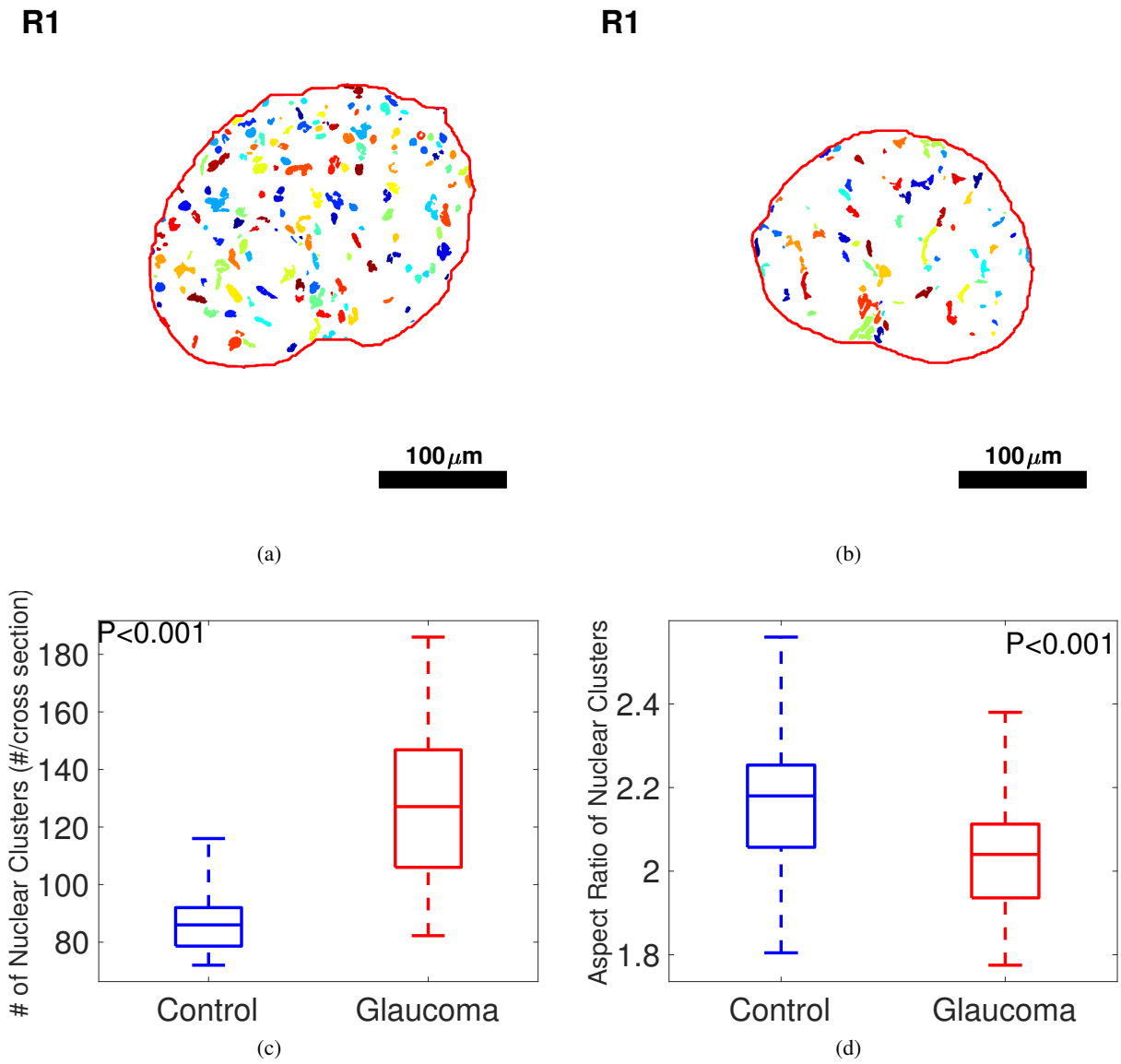

Figure 6: Comparison of nuclear clusters from a region-matched pair of ON sections, showing: individually labelled nuclear clusters of (a) 3-day OHT and (b) control nerve. Three-day OHT ON had (c) higher number of nuclear clusters, but (d) a lower aspect ratio of clusters in R1.

Table 3: Results from general linear models for comparison of measured outcomes among axial regions, showing the mean ratios of 3-day OHT over control outcomes and the Bonferroni adjusted $P-$values for pairwise ratio comparisons.
ON, GFAP, actin and nuclear area had ratios significantly higher than 1 in all axial regions. The ratios were higher in R1 than R2 and were not significant different between R2 and R3. Pairwise ratio comparisons with $P-$values that were not significant were marked as NS. In column 3-5, ratio values significantly different from 1 were highlighted with * for $P-\text{value} \leq 0.01$, and with ** for $P-\text{value} \leq 0.05$.

		Estimated Mean Ratio (95% CI)			**Adjusted *P*-value**	
	Measured Features	**R1**	**R2**	**R3**	**R1 vs R2**	**R1 vs R3**
GFAP	Aspect Ratio of ON (mm/mm)	1.05 (0.97, 1.12)	1.03 (0.97, 1.09)	1.00 (0.95, 1.05)	NS	NS
	ON Area (mm^2)	1.16 (1.10, 1.22) **	1.07 (1.03, 1.11) **	1.05 (1.02, 1.09) **	< 0.0003	< 0.0003
	GFAP Area (mm^2)	1.12 (1.04, 1.20) **	1.09 (1.00, 1.17) **	1.07 (0.99, 1.14) *	NS	NS
	GFAP Area Fraction (mm^2/mm^2)	0.96 (0.93, 1.00) **	1.00 (0.96, 1.05)	1.00 (0.95, 1.04)	0.01	NS
	GFAP Beam Anisotropy	1.51 (1.32, 1.71) **	1.89(1.39, 2.39) **	1.56 (1.04, 2.08) **	0.08	NS
	Process Width (μm)	0.97 (0.96, 0.98) **	0.98 (0.96, 1.01)	0.98 (0.94, 1.02)	NS	NS
	Process Width - cen (μm)	0.96 (0.95, 0.98) **	0.99 (0.94, 1.03)	0.97 (0.92, 1.02)	NS	NS
	Process Width - peri (μm)	0.97 (0.96, 0.99) **	0.99 (0.96, 1.02)	0.98 (0.94, 1.02)	NS	NS
	Process Width - rim (μm)	0.98 (0.96, 1.00) *	0.98 (0.94, 1.02)	0.96 (0.90, 1.03)	NS	NS
Actin	Actin Area (mm^2)	1.15 (1.09, 1.20) **	1.07 (1.03, 1.11) **	1.05 (1.01, 1.09) **	< 0.0003	< 0.0003
	Actin Area Fraction (mm^2/mm^2)	0.99 (0.98, 1.00)	0.995 (0.991, 0.998) **	1.00 (0.99, 1.01)	NS	NS
	Actin Process Anisotropy	1.13 (0.84, 1.41)	1.69 (1.14, 2.24) **	1.40 (1.11, 1.69) **	NS	NS
Axon	Axonal Area (mm^2)	1.13 (1.06, 1.20) **	1.04 (1.00, 1.08) **	1.06 (1.00, 1.12) *	0.002	0.05
	# of Axonal Compartments (#/cross section)	1.13 (1.05, 1.21) **	1.07 (0.98, 1.15)	1.05 (0.94, 1.15)	NS	NS
	Mean Area of Axonal Compartments (μm^2)	1.00 (0.90, 1.10)	0.99 (0.89, 1.11)	1.04 (0.90, 1.17)	NS	NS
Nuclei	Nuclear Area (mm^2)	1.27 (1.04, 1.51) **	1.19 (1.02, 1.36) **	1.16 (1.04, 1.28) **	NS	NS
	Nuclear Area Fraction (mm^2/mm^2)	1.13 (0.97, 1.29)	1.10 (1.00, 1.20) *	1.07 (0.97, 1.17)	NS	NS
	# of Nuclear Clusters (#/cross section)	1.38 (1.18, 1.58) **	1.30 (1.13, 1.47) **	1.25 (1.12, 1.37) **	0.02	NS
	Nuclear Cluster Density ($\#/mm^2$)	1.19 (1.06, 1.33) **	1.10 (1.08, 1.31) **	1.15 (1.05, 1.24) **	NS	NS
	Mean Area of Nuclear Clusters (μm^2)	0.93 (0.88, 0.99) **	0.92 (0.90, 0.95) **	0.98(0.94, 1.01)	NS	NS
	Mean Aspect Ratio of Nuclear Clusters ($\mu m/\mu m$)	0.93 (0.91, 0.96) **	0.99 (0.98, 1.00)	1.00 (0.98, 1.03)	< 0.0003	0.002

3.3 Morphological changes were associated with difference in final IOP

The ratios of 3-day OHT over control data in several measured parameters were correlated with the difference in IOP between 3-day OHT and control pairs (Supplemental Table S3). The enlargement of ON area increased with greater ΔIOP (Figure 7a). Similarly, the fold increase in GFAP area, and number of axonal compartments also increased with increased ΔIOP (Figure 7b & c). On the other hand, the GFAP processes in the central zone were thinner with larger ΔIOP (Figure 7d).

4 Discussion

4.1 Regional differences in control astrocyte morphology

We found differences in normal astrocyte structure between the region nearer to the eye (R1) and ON regions more cephalad. The overall average cross-sectional area of control mouse ON was 0.051 mm^2 with 123 nuclear clusters per section. Both of these are consistent with mean area of 0.04-0.06 mm^2 and 41-275 per section reported in Swiss black mice[34]. Our report documents detailed differences in the phenotype of R1 region astrocytes and their response to 3-day OHT. Most measured parameters were different after 3-day OHT in R1, the region known to be subject to IOP-generated stress in mouse ON, while features were similar to control values in R2 and R3, in which axonal transport blockade does not occur in mice or rats. In controls, the fractional area occupied by GFAP, as well as GFAP-labelled process width were greatest at BMO and declined toward the myelinated ON. This could be in part due to the addition of oligodendrocytes and myelin in R2 and R3; however, the decline in GFAP fraction was already evident through the intervals within R1 itself, before any myelination. The measured GFAP process thicknesses in R1 were slightly higher than the 1.30 μm reported by Lye-Barthel et al.[35]. We captured an average thickness of all GFAP processes, including those bordering the peripapillary sclera, while Lye-Barthel et al. measured thickness of 50 processes at a distance 10-15 μm away from the nucleus. The discrepancies could also be due to differences in animal models and strains of mice.

The actin area increased through R1 and its fractional area kept pace with the widening of the ON through R1. The configuration of actin bundles in R1 appeared to course straight from side to side of the ON, but were more convoluted in R2 and R3. The general pattern of straight processes bridging from one

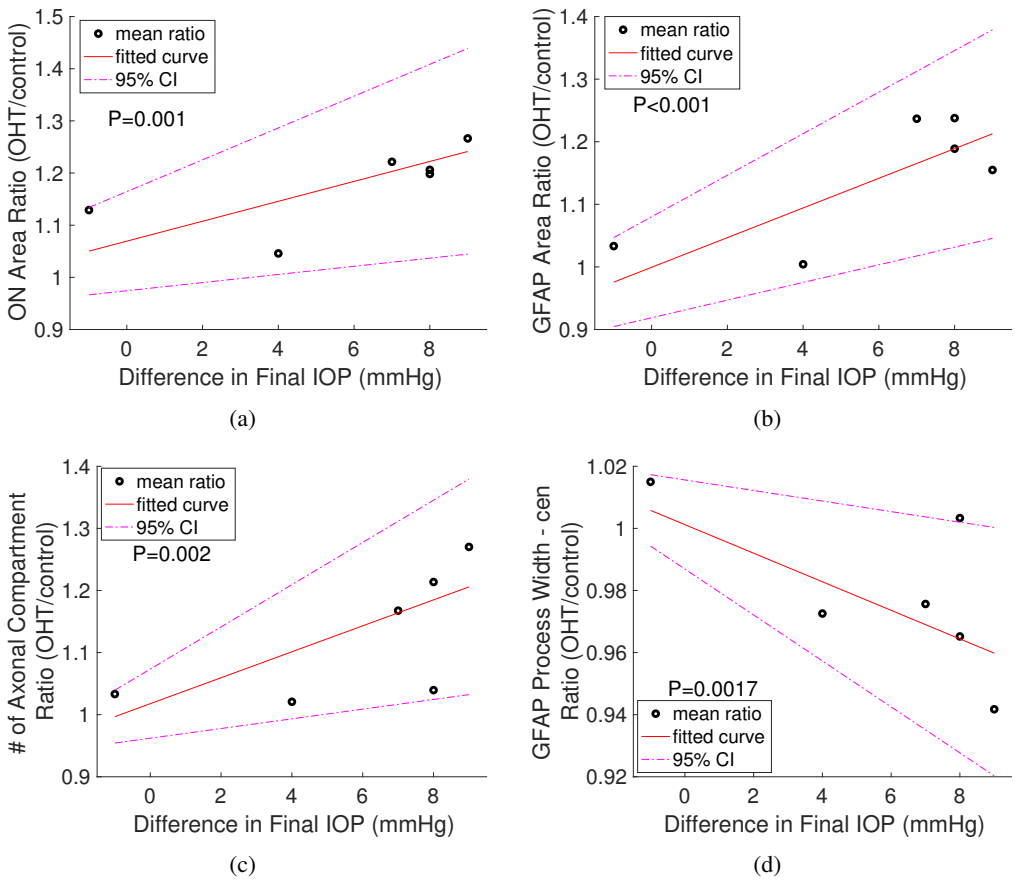

Figure 7: Ratio between 3-day OHT and control eye pairs for 4 parameters, calculated from each of the six 40μm-intervals in R1, was greater with larger IOP difference (ΔIOP) in (a) ON area, (b) GFAP area, and (c) number of axonal compartments, while the GFAP process width ratio was smaller with greater IOP difference (d). Each data point represent mean of the interval ratios in R1 from each mouse. The large variation in ratios for each mouse were due to large axial variations in R1, as shown in (Figure 3a-c). The correlation was analyzed using general linear models, which take into consideration correlations among repeat measurements in multiple intervals for a single ON.

side of the ON to the other is consistent with the configuration of individually labelled astrocytes reported by Sun et al.[36]. The actin morphology in the unmyelinated and myelinated regions resemble the configuration of connective tissues in human lamina cribriosa and myelinated ON, respectively[37]. The honeycomb shape of actin bundles in R1 is analogous to the laminar beams in human LC, the load bearing tissue at the ONH that protects retinal ganglion cell axons. The astrocytic actin fiber bundles were less straight further away from the BMO, coinciding with a more curved connective tissue pattern in the myelinated human ON.

Not only was the astrocytic network in R1 different from R2 and R3, but we found, for the first time to our knowledge, quantitative specializations of astrocyte process structure among the central, peripheral and rim zones of control mouse ONH. Astrocyte processes were large near the cell soma, branched repeatedly, and interdigitate as small end processes within the axonal bundles. However, GFAP-labelled processes were thickest as they contacted their basement membranes in the rim zone of the ON at the peripapillary sclera. Likewise, the fractional area occupied by astrocyte processes was greatest at the rim zone and thicker in the mid-peripheral zone compared to the center of the ON. This regional morphology is compatible with the appearance of astrocyte processes at the rim zone as viewed by transmission electron microscopy[38]. In that work, we showed that astrocytes processes widen to form shapes similar to architectural pillars, much as retinal Muller glia do at the internal limiting membrane. At that location, they form electron dense junctional complexes along the cell membrane facing their basement membrane. Furthermore, they are heavily interdigitated with the basement membrane zone in R1, seemingly to increase the ability to withstand hoop stress generated by IOP through the sclera. Astrocytes further from BMO do not exhibit either these interdigitations or the junctional complexes at the ON periphery.

4.2 Changes in astrocyte morphology with IOP elevation

Three-day OHT nerves had greater ON, actin, axon compartments, and nuclear areas in R1, R2 and R3, but the increases were remarkably greater in the unmyelinated R1. The observed increase in ON area in R1 aligned with prior studies[39]. There were also decreases in GFAP-labelled fractional area and process width and an increase in number of axonal compartments and axonal area in R1. These changes are consistent with known axon swelling caused by axonal transport obstruction as well as with the reported extension of new astrocyte processes with IOP elevation[17]. R1 is the region in which transport obstruction occurs in

mice[40], measured by accumulation of amyloid precursor protein[33], reduction in mitochondrial mobility[7], and decrease in neurofilament[41,42]. The swelling of axons with acute IOP elevation in the bead injection model has been well-documented[43]. The transport block in the mouse ON is present more posteriorly than in larger mammals and is shared by rats after IOP elevation. In larger mammalian eyes and humans, anterograde and retrograde transport block in axons occurs in the connective tissue zone of the lamina cribrosa and myelination begins just posterior to this[42,44–47]. Interestingly, despite the much larger size of human eyes, the region in which transport block occurs is around 240 μm long in both human and mouse eyes. We found that the larger the degree of IOP elevation relative to the baseline, the larger were the morphological changes. Larger study groups with more detailed IOP measures over longer periods are needed to verify the associations now that this model system has shown promise.

GFAP is one component of the intermediate filaments (IFs) and has 10 isoforms. The astrocyte IFs are comprised of all isoforms of GFAP, along with vimentin and nestin[48]. IFs can shorten, elongate, and rearrange by polymerization and depolymerization[49], regulated by phosphorylation, with exchange between soluble monomers, short fragments, and an assembled GFAP network[50]. As globular proteins that lack enzymatic activity[51], IFs have no associated molecular motors or contractile properties[52], but are more flexible and stretchable than actin[53]. They contribute to focal cell adhesions involving integrin-mediated signaling through Rho GTPases and ROCK. Nestin controls focal adhesion kinase recruitment to focal adhesions and regulates integrin clustering. Vimentin and GFAP regulate endocytosis and endosome motility in astrocytes, and under stress, IF expression is frequently increased[52]. Stress in cultured astrocytes produced increased GFAP[54]. We also found increased GFAP coverage in 3-day OHT mouse. However, no increase in GFAP gene expression occurred in either rat nor in mouse glaucoma[16,55,56]. In rat glaucoma, GFAP was reportedly downregulated[57]. This along with the decline of the fractional area of GFAP-labelled astrocyte processes in R1 shown in our study, suggest that the increase in coverage was a result of redistribution of overlapping GFAP. Redistribution of filaments after increase in hydrostatic pressure has also been shown in cultured human astrocytes[58].

There were also IOP-induced, significant alterations in actin parameters and nuclear clusters with IOP increase. The fractional actin area increased, keeping pace with an overall increase in ON area, in contrast to the relative decrease in GFAP fractional area. Brain astrocytes express smooth muscle action (αSMA)

under pathological conditions[59–61]. Clark et al[62] found that human, fibroblast-like, lamina cribrosa cells in culture express cross-linked actin networks when stimulated by corticosteroid, but human astrocyte cultures did not. In separate research[38], we observed that 3-day IOP elevation in mouse leads to increased αSMA in R1 astrocytes. Thus, the maintenance of fractional actin area with expansion of the ON area is consistent with an actual increase in total actin cytoskeleton as an early response to IOP increase. The actin retrograde flow is mediated by IFs that accumulate asymmetrically around the nuclear envelope[63] and perturbations of the IF network alter nuclear positioning in astrocytes[49]. These mechanisms may be involved in the changes in nuclear clusters that we observed.

From a biomechanical perspective, the cytoskeleton provides structural properties for cells, and the expression of GFAP and actin are correlated with tissue stiffness in murine glial cells[64–66]. Rearrangement of the actin cytoskeleton stimulated by hydrostatic pressure or other forms of mechanical stress is known to be a mechanotranslational response in different cell types[19,67–69]. Astrocytes in the optic nerve head express mechanosensitive channels[70], whose effects may alter the cytoskeleton. The actin cytoskeleton is also important for cytoskeleton-based vesicle mobility and forward trafficking of Connexin 43, and for calcium signaling, cell motility and cell adhesion[20,71–73]. In neurodegenerative diseases, actin reorganization occurs[74] and in experimental and human glaucoma, astrocytes move to fill ONH pores previously occupied by axons[1]. While axonal loss is not present within 3 days in the bead injection model, actin reorganization may represent an initial result of IOP-produced strain. It could also be partly due to the extension of new fine processes[17]. The newly described junctional complexes present at astrocyte processes facing their basement membrane at the peripapillary sclera[38] are integrin- and dystroglycan-linked through the cell membrane to the actin network, altering its configuration as a response to mechanical stress.

There were, in addition, alterations in the number, and likely the orientation, of astrocytes with IOP increase. The number of nuclear clusters increased dramatically, while their mean size decreased. This could have in part resulted from separation of existing, originally closely apposed nuclei, which may be more overlapping in the images of control ON, but separate as the ON expands in the treated ON. However, we have found significant astrocyte proliferation by Ki67 labeling in mice one week after IOP elevation[38] and in rat glaucoma models[75]. Thus, some of the increase in nuclear clusters may be actual increase in astrocyte numbers. Since external stresses are transmitted from the plasma membrane via the cytoskeleton to

the nucleus, a change in nuclear shape or conformation is expected, as we observed and has been previously reported[76,77]. The nuclear clusters were found to be less elongated and smaller in size, which suggests possible reorientation of the cell and nucleus toward the long axis of the nerve.

The effects of IOP elevation were differentially greater in the central ON than at the rim zone. In control ON, astrocyte processes were thinner in the central zone than peripherally and in the rim. The thicker rim zone processes adjoin the astrocyte basement membrane zone. As the astrocytic network serves to withstand both trans-lamina axial stress and circumferential hoop stress along the ON, larger processes in the rim zone help to reinforce them against the stress concentration induced by IOP. Overall, the GFAP processes became more in parallel with each other after 3-day OHT, which could give rise to a smaller IOP-induced strain response along the aligned direction compare to that in the direction perpendicular to the alignment. However, this was only a relative change and both actin fiber bundles and GFAP-labelled processes in R1 maintained transverse alignment spanning the OHT nerves. Since actin is known to extend fibers to align with the direction of stress, this confirmed that hoop stress is a significant component in the astrocytic network. With IOP elevation, process thickness in central and peripheral zones decreased significantly, while processes in the rim zone did not significantly change. This is consistent with our finding that IOP-induced strain responses are greater in the central ON of mice than in the periphery with ex-vivo inflation testing[78].

There were limitations in this study. While GFAP served as an astrocyte-specific indicator in the ONH, phalloidin and DAPI stains are nonspecific to astrocytes. Other types of cell such as microglia, capillary endothelium and pericytes are present in the ON, though they represent a small fraction of all cells. Recent study of rat ONH showed that ON consists of 78% astrocytes[75]. GFAP antibodies have limited depth penetration in sections, necessitating our image capture from the more superficial layer of each section. To account for artifact in some sections, we calculated an average data per 40 μm interval. The acquired signals were thresholded and binarized for quantitative measurements, potentially eliminating the variations in signal brightness and, hence, the nonuniformity of cytoskeletal proteins across the cytoplasm. The axonal compartments were inferred from negative space of binarized actin and nuclear images, which could include extracellular fluids or voids. However, these should not interfere with valid comparisons of the relative differences between OHT and control ON. To ensure that the images were adequately processed, the GFAP,

actin and nuclear area fractions calculated from a local region of the binarized images were compared to that from manual tracings. The average absolute percentage difference in area fractions from the custom algorithm compare to that from the manual segmentation was 6.8%, slightly lower than the percentage difference between two manual tracings of the nuclear channels by the same operator (7.1%). The method was applied to only one time point after IOP elevation, prior to detectable axonal loss. Some of the changes may be reversible if IOP were lowered, or may progress to further changes with longer observation periods. We studied the changes in the cellular, astrocytic lamina, but are approaching alterations in the adjoining peripapillary sclera with other methods. Contributions from the mechanical response of the sclera are likely to be as important to effects of IOP on glaucoma damage as the astrocyte responses.

5 Conclusion

A total of 18 structural features were measured in 6 pairs of control and OHT mouse optic nerves. The structural features measured in cross sections were found to vary with axial location, region, and to be correlated with degree of IOP change. Specifically, the main findings include:

1. Major differences after 3-day OHT treatment occurred in the unmyelinated ON region but not in the myelin-transition and myelinated regions.

2. GFAP processes were thicker in the rim region compared to the central and peripheral zones. Within the unmyelinated region, processes became thinner in the central and peripheral zones after 3-day OHT.

3. The measured ON, GFAP, actin and nuclear areas were greater in 3d-OHT ONs in the unmyelinated region, but the GFAP area fraction was lower. The processes also became more aligned along an average process direction.

4. The differences between 3-day OHT and control nerves in some measured outcomes increased with larger IOP difference.

Overall, changes in the astrocytic network could affect the local biomechanical and physiological support for RGC axons and may be predictive of the susceptibility to glaucomatous axonal damage.

6 Acknowledgement

This work was supported by: NIH EY 02120 (Dr Quigley); EY 01765 (Core facility grant, Wilmer Institute); unrestricted donations to the Glaucoma Center of Excellence, Wilmer Institute; NSF Award 1727104; Brightfocus Foundation G2015132; and the Croucher Foundation (YTTL).

Disclosures

The authors declare that they have no conflicts of interest.

References

[1] Quigley HA, Addicks EM, Green WR, Maumenee AE. Optic nerve damage in human glaucoma: II. The site of injury and susceptibility to damage. *Arch Ophthalmol.* 1981; 99:635–649.

[2] Leske MC, Heijl A, Hussein M, Bengtsson B, Hyman L, Komaroff E. Factors for glaucoma progression and the effect of treatment: The early manifest glaucoma trial. *Arch Ophthalmol.* 2003; 121:48–56.

[3] Quigley HA, Green WR. The Histology of Human Glaucoma Cupping and Optic Nerve Damage: Clinicopathologic Correlation in 21 Eyes. *Ophthalmol.* 1979; 86:1803–1827.

[4] Gaasterland D, Kupfer C. Experimental glaucoma in the rhesus monkey. *Invest Ophthalmol Vis Sci.* 1974; 13:455–457.

[5] Bunt-Milam AH, Dennis MB, Bensinger RE. Optic nerve head axonal transport in rabbits with hereditary glaucoma. *Exp Eye Res.* 1987; 44:537–551.

[6] Morrison JC, Dorman Pease ME, Dunkelberger GR, Quigley HA. Optic Nerve Head Extracellular Matrix in Primary Optic Atrophy and Experimental Glaucoma. *Arch Ophthalmol.* 1990; 108:1020–1024.

[7] Kimball EC, Jefferys JL, Pease ME, et al. The effects of age on mitochondria, axonal transport, and axonal degeneration after chronic IOP elevation using a murine ocular explant model. *Exp Eye Res.* 2018; 172:78–85.

[8] Chidlow G, Ebneter A, Wood JPM, Casson RJ. The optic nerve head is the site of axonal transport disruption, axonal cytoskeleton damage and putative axonal regeneration failure in a rat model of glaucoma. *Acta Neuropathol.* 2011; 121:737–751.

[9] Voorhees AP, Jan NJ, Sigal IA. Effects of collagen microstructure and material properties on the deformation of the neural tissues of the lamina cribrosa. *Acta Biomat.* 2017; 58:278–290.

[10] Zhang L, Albon J, Jones H, et al. Collagen microstructural factors influencing optic nerve head biomechanics. *Invest Ophthalmol Vis Sci.* 2015; 56:2031–2042.

[11] Schwaner SA, Kight AM, Perry RN, et al. A methodology for individual-specific modeling of rat optic nerve head biomechanics in glaucoma. *J Biomech Eng.* 2018; 140.

[12] Simard M, Nedergaard M. The neurobiology of glia in the context of water and ion homeostasis. *Neurosci.* 2004; 129:877–896.

[13] Martin DL. Synthesis and release of neuroactive substances by glial cells. *Glia.* 1992; 5:81–94.

[14] Parpura V, Basarsky TA, Liu F, Jeftinija K, Jeftinija S, Haydon PG. Glutamate-mediated astrocyte-neuron signalling. *Nature.* 1994; 369:744–747.

[15] Sun D, Lye-Barthel M, Masland RH, Jakobs TC. Structural remodef of fibrous astrocytes after axonal injury. *J Neurosci.* 2010; 30:14008–14019.

[16] Sun D, Qu J, Jakobs TC. Reversible reactivity by optic nerve astrocytes. *Glia.* 2013; 61:1218–1235.

[17] Wang R, Seifert P, Jakobs TC. Astrocytes in the optic nerve head of glaucomatous mice display a characteristic reactive phenotype. *Invest Ophthalmol Vis Sci.* 2017; 58:924–932.

[18] Hernandez MR. The optic nerve head in glaucoma: Role of astrocytes in tissue remodeling. *Prog Retin Eye Res.* 2000; 19:297–321.

[19] Tehrani S, Davis L, Cepurna WO, et al. Astrocyte structural and molecular response to elevated intraocular pressure occurs rapidly and precedes axonal tubulin rearrangement within the optic nerve head in a rat model. *PLoS One.* 2016; 11:1–22.

[20] Potokar M, Kreft M, Li L, et al. Cytoskeleton and vesicle mobility in astrocytes. *Traffic.* 2007; 8:12–20.

[21] Tao J, Li Y, Vig DK, Sun SX. Cell mechanics: a dialogue. *Rep Prog Phys.* 2017; 80:036601.

[22] Pollard TD, Cooper JA. Actin, a central player in cell shape and movement. 2009.

[23] Ling YTT, Shi R, Midgett DE, Jefferys JL, Quigley HA, Nguyen TD. Characterizing the collagen network structure and pressure-induced strains of the human lamina cribrosa. *Invest Ophthalmol Vis Sci.* 2019; 60:2406–2422.

[24] Zhuo L, Sun B, Zhang CL, Fine A, Chiu SY, Messing A. Live astrocytes visualized by green fluorescent protein in transgenic mice. *Dev Biol.* 1997; 187:36–42.

[25] Regan MR, Huang YH, Kim YS, et al. Variations in promoter activity reveal a differential expression and physiology of glutamate transporters by glia in the developing and mature CNS. *J Neurosci.* 2007; 27:6607–6619.

[26] Cone FE, Gelman SE, Son JL, Pease ME, Quigley HA. Differential susceptibility to experimental glaucoma among 3 mouse strains using bead and viscoelastic injection. *Exp Eye Res.* 2010; 91:415–424.

[27] Barthel LK, Raymond PA. Improved method for obtaining 3-microns cryosections for immunocytochemistry.. *J Histochem Cytochem.* 1990; 38:1383–1388.

[28] Zuiderveld K. Contrast limited adaptive histogram equalization. *Graph Gem.* 1994:474–485.

[29] Otsu N. A threshold selection method from gray-level histograms. *IEEE Trans Syst Man Cybern.* 1979; 9:62–66.

[30] D'Amore A, Stella JA, Wagner WR, Sacks MS. Characterization of the complete fiber network topology of planar fibrous tissues and scaffolds. *Biomaterials.* 2010; 31:5345–5354.

[31] Petroll WM, Cavanagh HD, Barry P, Andrews P, Jester JV. Quantitative analysis of stress fiber orientation during corneal wound contraction. *J Cell Sci.* 1993; 104:353–363.

[32] Berens P. CircStat: a MATLAB toolbox for circular statistics. *J Stat Softw.* 2009; 31:1–21.

[33] Korneva A, Schaub JA, Jefferys JL, et al. A method to quantify regional axonal transport blockade at the optic nerve head after short term intraocular pressure elevation in mice. *Exp Eye Res.* 2020:108035.

[34] Mabuchi F, Aihara M, Mackey MR, Lindsey JD, Weinreb RN. Optic nerve damage in experimental mouse ocular hypertension. *Invest Ophthalmol Vis Sci.* 2003; 44:4321–4330.

[35] Lye-Barthel Ming, Sun Daniel, Jakobs Tatjana C. Morphology of astrocytes in a glaucomatous optic nerve. *Invest Ophthalmol Vis Sci.* 2013; 54:909–917.

[36] Sun Daniel, Lye-Barthel Ming, Masland Richard H, Jakobs Tatjana C. The morphology and spatial arrangement of astrocytes in the optic nerve head of the mouse. *J Comp Neurol.* 2009; 516:1–19.

[37] Jeffery G, Evans A, Albon J, Duance V, Neal J, Dawidek G. The human optic nerve: fascicular organisation and connective tissue types along the extra-fascicular matrix. *Anat and Embryol.* 1995; 191:491–502.

[38] Quillen S, Schaub J, Quigley HA, Pease ME, Korneva A, Kimball EC. Astrocyte Responses to Experimental Glaucoma in Mouse Optic Nerve Head . *Investigative Ophthalmology and Visual Science.* 2020; (under review).

[39] Nguyen C, Midgett D, Kimball EC, et al. Measuring deformation in the mouse optic nerve head and peripapillary sclera. *Invest Ophthalmol Vis Sci.* 2017; 58:721–733.

[40] Howell GR, Libby RT, Jakobs TC, et al. Axons of retinal ganglion cells are insulted in the optic nerve early in DBA/2J glaucoma. *J Cell Biol.* 2007; 179:1523–1537.

[41] Schaub JA, Kimball EC, Steinhart MR, et al. Regional retinal ganglion cell axon loss in a murine glaucoma model. *Invest Ophthalmol Vis Sci.* 2017; 58:2765–2773.

[42] Buckingham BP, Inman DM, Lambert W, et al. Progressive ganglion cell degeneration precedes neuronal loss in a mouse model of glaucoma. *J Neurosci.* 2008; 28:2735–2744.

[43] Kimball Elizabeth C, Pease Mary E, Steinhart Matthew R, et al. A mouse ocular explant model that enables the study of living optic nerve head events after acute and chronic intraocular pressure elevation: Focusing on retinal ganglion cell axons and mitochondria. *Exp Eye Res.* 2017; 160:106–115.

[44] Anderson DR, Hendrickson A. Effect of intraocular pressure on rapid axoplasmic transport in monkey optic nerve. *Invest Ophthalmol Vis Sci.* 1974; 13:771–783.

[45] Minckler DS, Bunt AH, Johanson GW. Orthograde and retrograde axoplasmic transport during acute ocular hypertension in the monkey.. *Invest Ophthalmol Vis Sci.* 1977; 16:426–441.

[46] Quigley HA, Green WR. The histology of human glaucoma cupping and optic nerve damage: clinicopathologic correlation in 21 eyes. *Ophthalmol.* 1979; 86:1803–1827.

[47] Quigley HA, Addicks EM. Chronic experimental glaucoma in primates. II. Effect of extended intraocular pressure elevation on optic nerve head and axonal transport.. *Invest Ophthalmol Vis Sci.* 1980; 19:137–152.

[48] Moeton M, Stassen OMJA, Sluijs JA, et al. GFAP isoforms control intermediate filament network dynamics, cell morphology, and focal adhesions. *Cell Mol Life Sci.* 2016; 73:4101–4120.

[49] Leduc C, Etienne-Manneville S. Regulation of microtubule-associated motors drives intermediate filament network polarization. *J Cell Biol.* 2017; 216:1689–1703.

[50] Hol EM, Capetanaki Y. Type III intermediate filaments desmin, glial fibrillary acidic protein (GFAP), vimentin, and peripherin. *Cold Spring Harb Perspect Biol.* 2017; 9:a021642.

[51] Herrmann H, Aebi U. Intermediate filaments: structure and assembly. *Cold Spring Harb Perspect Biol.* 2016; 8:a018242.

[52] Etienne-Manneville S. Cytoplasmic intermediate filaments in cell biology. *Annu Rev Cell and Dev Bi.* 2018; 34:1–28.

[53] Block J, Schroeder V, Pawelzyk P, Willenbacher N, Köster S. Physical properties of cytoplasmic intermediate filaments. *Biochim Biophys Acta (BBA)-Mol Cell Res.* 2015; 1853:3053–3064.

[54] Varela HJ, Hernandez MR. Astrocyte responses in human optic nerve head with primary open-angle glaucoma.. *Journal of glaucoma.* 1997; 6:303–313.

[55] Johnson EC, Jia L, Cepurna WO, Doser TA, Morrison JC. Global changes in optic nerve head gene expression after exposure to elevated intraocular pressure in a rat glaucoma model. *Invest Ophthalmol Vis Sci.* 2007; 48:3161–3177.

[56] Qu J, Jakobs T. The time course of gene expression during reactive gliosis in the optic nerve. *Invest Ophthalmol Vis Sci.* 2013; 54:5586–5586.

[57] Johnson EC, Deppmeier LMH, Wentzien SKF, Hsu I, Morrison JC. Chronology of optic nerve head and retinal responses to elevated intraocular pressure. *Invest Ophthalmol Vis Sci.* 2000; 41:431–442.

[58] Salvador-Silva M, Ricard CS, Agapova OA, Yang P, Hernandez MR. Expression of small heat shock proteins and intermediate filaments in the human optic nerve head astrocytes exposed to elevated hydrostatic pressure in vitro. *J Neurosci Res.* 2001; 66:59–73.

[59] Pekny M. Astrocytic intermediate filaments: lessons from GFAP and vimentin knock-out mice. in *Prog Brain Res*; 132:23–30Elsevier2001.

[60] Moreels M, Vandenabeele F, Dumont D, Robben J, Lambrichts I. Alpha-smooth muscle actin (α-SMA) and nestin expression in reactive astrocytes in multiple sclerosis lesions: potential regulatory role of transforming growth factor-beta 1 (TGF-β1). *Neuropath Appl Neuro.* 2008; 34:532–546.

[61] Vedrenne N, Sarrazy V, Richard L, et al. Isolation of astrocytes displaying myofibroblast properties and present in multiple sclerosis lesions. *Neurochem Res.* 2017; 42:2427–2434.

[62] Tovar-Vidales T, Wordinger RJ, Clark AF. Identification and localization of lamina cribrosa cells in the human optic nerve head. *Exp Eye Res.* 2016; 147:94–97.

[63] Dupin I, Sakamoto Y, Etienne-Manneville S. Cytoplasmic intermediate filaments mediate actin-driven positioning of the nucleus. *J Cell Sci.* 2011; 124:865–872.

[64] Lu YB, Iandiev I, Hollborn M, et al. Reactive glial cells: increased stiffness correlates with increased intermediate filament expression. *FASEB J.* 2011; 25:624–631.

[65] Moeendarbary E, Weber IP, Sheridan GK, et al. The soft mechanical signature of glial scars in the central nervous system. *Nat Commun.* 2017; 8:1–11.

[66] Maneshi MM, Sachs F, Hua SZ. Heterogeneous cytoskeletal force distribution delineates the onset Ca2+ influx under fluid shear stress in astrocytes. *Front Cell Neurosci.* 2018; 12:69.

[67] Haskin C, Cameron I. Physiological levels of hydrostatic pressure alter morphology and organization of cytoskeletal and adhesion proteins in MG-63 osteosarcoma cells. *Biochem Cell Bio.* 1993; 71:27–35.

[68] Girard PR, Nerem RM. Shear stress modulates endothelial cell morphology and F-actin organization through the regulation of focal adhesion-associated proteins. *J Cell Physiol.* 1995; 163:179–193.

[69] Ohashi K, Fujiwara S, Mizuno K. Roles of the cytoskeleton, cell adhesion and rho signalling in mechanosensing and mechanotransduction. *J Biochem.* 2017; 161:245–254.

[70] Choi HJ, Sun D, Jakobs TC. Astrocytes in the optic nerve head express putative mechanosensitive channels. *Mol Vis.* 2015; 21:749–766.

[71] Smyth JW, Vogan JM, Buch PJ, et al. Actin cytoskeleton rest stops regulate anterograde traffic of connexin 43 vesicles to the plasma membrane. *Circ Res.* 2012; 110:978–989.

[72] John GR, Chen L, Rivieccio MA, Melendez-Vasquez CV, Hartley A, Brosnan CF. Interleukin-1β induces a reactive astroglial phenotype via deactivation of the Rho GTPase–Rock axis. *J Neurosci.* 2004; 24:2837–2845.

[73] Cotrina ML, Lin JHC, Nedergaard M. Cytoskeletal assembly and ATP release regulate astrocytic calcium signaling. *J Neurosci.* 1998; 18:8794–8804.

[74] Hansson E. Actin filament reorganization in astrocyte networks is a key functional step in neuroinflammation resulting in persistent pain: novel findings on network restoration. *Neurochem Res.* 2015; 40:372–379.

[75] Lozano DC, Choe TE, Cepurna WO, Morrison JC, Johnson EC. Early optic nerve head glial proliferation and jak-stat pathway activation in chronic experimental glaucoma. *Invest Ophthalmol Vis Sci.* 2019; 60:921–932.

[76] Kim DH, Li B, Si F, Phillip JM, Wirtz D, Sun SX. Volume regulation and shape bifurcation in the cell nucleus. *J Cell Sci.* 2015; 128:3375–3385.

[77] Seirin-Lee S, Osakada F, Takeda J, et al. Role of dynamic nuclear deformation on genomic architecture reorganization. *PLoS Comput Biol.* 2019; 15.

[78] Korneva A, et al . Regional Mechanical Strains in Mouse Astrocytic Lamina and Peripapillary Sclera after Chronic IOP Elevation. *IOVS.* 2020; E-Abstract 3366034.